Nonlinear interaction between bulk point vortices and an unstable interface with nonuniform velocity shear such as Richtmyer-Meshkov instability

Nonlinear interaction between bulk point vortices and an unstable interface with nonuniform velocity shear such as Richtmyer–Meshkov instability

Chihiro Matsuoka, Katsunobu Nishihara

Physics of Plasmas ARTICLE scitation.org/journal/php

Nonlinear interaction between bulk point vortices and an unstable interface with nonuniform velocity shear such as Richtmyer–Meshkov instability

Cite as: Phys. Plasmas **27**, 052305 (2020); doi: 10.1063/1.5131701
Submitted: 15 October 2019 · Accepted: 11 May 2020 ·
Published Online: 28 May 2020

Chihiro Matsuoka[1,a] and Katsunobu Nishihara[1,2]

AFFILIATIONS

[1]Laboratory of Applied Mathematics, Graduate School of Engineering, Osaka City University, Sugimoto, Sumiyoshi, Osaka 558-8585, Japan
[2]Institute of Laser Engineering, Osaka University, Suita, Osaka 565-0871, Japan

[a]**Present address:** Nambu Yoichiro Institute of Theoretical and Experimental Physics (NITEP), Osaka City University, Osaka City University Advanced Mathematical Institute (OCAMI), Osaka, Japan. **Author to whom correspondence should be addressed:** cmatsuoka@osaka-cu.ac.jp

ABSTRACT

The nonlinear interaction between bulk point vortices and a vortex sheet with initially nonuniform velocity shear is investigated theoretically and numerically by use of the vortex method, taking the incompressible Richtmyer–Meshkov instability as an example. As the point vortices approach the interface, i.e., a nonuniform vortex sheet, they increase the local sheet strength of the vortex sheet, which causes different types of interface deformation depending on the sign of their circulation of point vortices. For example, when the circulation of a point vortex is the opposite sign of the local sheet strength, it induces a new type of vortex pair with an local enhanced sheet vortex. We refer to that as a pseudo-vortex pair in the current study. The pseudo-vortex pair creates a local satellite mushroom at the fully nonlinear stage. The obtained results indicate that the complexity of the interface structure is enhanced if the bulk vortices exist.

I. INTRODUCTION

The interaction of vortices with an interface plays an important role in a wide range of engineering, geophysics, and astrophysical flows. The interaction between a free surface and a vortex pair is one of the typical models to analyze the surface disturbances produced in the wake of a ship and/or the vortices shed by propellers, and this has been studied by various researchers experimentally[1,2] and theoretically.[1,3–5] Tyvand[4,5] reported that point vortices change their direction of motion due to the presence of a surface, while the surface elevation is also affected by point vortices if the vortices are strong. Similar results are also confirmed in numerical calculations by Telste.[3]

The interaction of a free surface and point vortices is also applicable to the problem of strong wind waves over a water surface.[6] Surface ocean waves are known to be excited by the wind.[7,8] It is reported that this excitation can be extremely strong if tiny vortices exist in the neighborhood of the water surface.[9] This study suggests that when a large vortex such as a hurricane and satellite vortices coexist, the system can be a turbulent state. This is a kind of stratified multi-layer system consisting of vortex sheets with point vortices in the air and a water surface, which should be investigated in the future.

Even apart from the above geophysical problems, there exist problems for the interaction between bulk vortices and an interface with strong vorticity in the field of plasma physics and astrophysics such as those represented by the Richtmyer–Meshkov instability (RMI).[10,11] RMI is a shock-induced density-stratified interfacial instability, and it is important in astrophysics[12–16] and inertial confinement fusion (ICF).[17,18] In supernova remnants (SNRs), RMI causes the amplification of magnetic field up to milligauss order.[12] The presence of a milligauss magnetic field has a crucial meaning in the long-standing paradigm of cosmic-ray proton acceleration in young SNRs. Extension of the present model to MHD RMI[15] is possible under certain assumptions. Mixing by RMI was also observed in gaseous interfaces.[19,20] Many references of RMI in experimental and theoretical studies are found in the review by Zhou.[21]

Nonuniform velocity shears are induced at the interface due to the passage of a shock wave across a corrugated interface in RMI.[22–27] Also, due to the conservation of tangential velocity at the rippled shock fronts, transverse velocity perturbations are generated inside the compressed fluids, which account for vorticity generation in the bulks.[23,25,28–34] Cobos-Campos and Wouchuk[34,35] reported that bulk vortices with sufficiently small vorticity stabilize the interfacial instability, at least in the (compressible) linear stage.[25,30–34] When the incident shock is strong and/or the amplitude of initial perturbations is large, it is known that a lot of vortices are left behind with the transmitted shock.[23,26,36] These bulk vortices can interact with the interface and they affect the vorticity distribution on the interface.

In real physical systems, multi-shocks propagate through a multi-layer target for high-density fuel compression in ICF.[37,38] Shock waves leave bulk vortices behind that. Defects in a laser fusion target[39] may also cause the generation of point-like vortices in bulk when shocks pass through. The vorticity of these bulk vortices may not always be weak, and the bulk vortices interact with the unstable interface with nonuniform velocity shear. With these problems in mind, we theoretically examine the nonlinear interaction between a nonuniform vortex sheet and bulk point vortices in the present paper.

The numerical method such as the vortex method[40] has developed as a high-precision computational method to investigate Kelvin–Helmholtz instability (KHI).[41,42] Extending this vortex method to the fluid systems with density stratification, Matsuoka and Nishihara[43–45] and Sohn *et al.*[46,47] succeeded in capturing the long-time behavior of the vortex sheet motion with density stratification such as the Rayleigh–Taylor instability (RTI) or RMI. These works assume that there are no vortices in bulk. However, in problems of practical importance, there exist bulk vortices as described above, and they strongly interact with an interface or a vortex sheet.

The simplest way to model vortex interaction with an interface is to assume the flow to be irrotational except at the location of point vortices and the interface. Point vortices correspond to singular points in the flow field, which mathematically have measure zero.[48,49] Developing an analytical model for water waves by Ablowitz *et al.*,[50] Curtis and Kalisch[51] calculated the nonlinear motion of point vortices with a free surface and a bottom, by use of a dealiased spectral method and a high-order time-stepping scheme.[51] They succeeded in capturing various complicated loci of point vortices moving under the influence of a surface with a boundary. In these water wave problems, the point vortices are under the air–water interface, and the initial vortex sheet strength of the interface is assumed to be approximately zero or extremely weak.

As with the above studies, we treat the potential flow problem, i.e., the incompressible and irrotational flow. The interaction between an interface with nonuniform velocity shear and bulk vortices has not been treated in the conventional vortex method; however, it is possible, and all physical quantities in bulk are computable if the flow is assumed potential. In the current study, we extend the vortex method for computations of interfacial dynamics to calculations of the whole region and investigate the interaction of an interface with bulk point vortices.

We show that when the point vortices approach the nonuniform vortex sheet, they create a new velocity shear, and the velocity shear produces nonuniform vortex sheet strength forming a vortex core,[52] where the velocity shear takes its maximum value in absolute values. Under certain conditions, the vortex core and the point vortex form a pseudo-vortex pair on the interface. We also show that finer structures such as satellite bubbles or satellite spikes appear on the interface due to the nonlinear interaction between bulk vortices and a nonuniform vortex sheet.

This paper is organized as follows. We provide the mathematical model when an interface with nonuniform velocity shear and bulk point vortices coexist in the system and derive the governing equations to describe their motion in Sec. II. In Sec. III, we present some numerical results for the motion of the vortex sheet and point vortices in RMI. Section IV is devoted to conclusion and discussions. The numerical scheme adopted in the current study is provided in Appendix A.

II. DERIVATION OF GOVERNING EQUATIONS

In this section, we present a mathematical model to investigate the interaction of bulk point vortices and a vortex sheet. We consider a fluid interface with density and tangential velocity jumps in two-dimensional inviscid and incompressible flows. We assume that the fluid is irrotational except the interface and point vortices. Then, the system is described by the potential flow, and the Bernoulli equation, i.e., the pressure continuous condition holds at the interface[24,43]

$$(1-A)\left\{\frac{\partial\phi_1}{\partial t}+\frac{1}{2}\left[\left(\frac{\partial\phi_1}{\partial x}\right)^2+\left(\frac{\partial\phi_1}{\partial y}\right)^2\right]\right\} = (1+A)\left\{\frac{\partial\phi_2}{\partial t}+\frac{1}{2}\left[\left(\frac{\partial\phi_2}{\partial x}\right)^2+\left(\frac{\partial\phi_2}{\partial y}\right)^2\right]\right\}, \quad (1)$$

where ϕ_i $(i=1, 2)$ is the velocity potential that is related to the fluid velocity $\boldsymbol{u}_i$ as $\boldsymbol{u}_i=\nabla\phi_i$ and A is the Atwood number defined by $A=(\rho_2-\rho_1)/(\rho_1+\rho_2)$, ρ_i the fluid density, and we denote $i=1$ $(i=2)$ as the lower (upper) fluid. Here, we assume that $i=1$ $(i=2)$ is the heavier (lighter) fluid. The Laplace equation $\triangle\phi_i=0$ $(i=1, 2)$ holds in each fluid region i.

As will be shown below, we consider here an interface that has initially sinusoidal velocity shear with the maximum value of the difference of tangential velocity between the lower and upper fluids, $2v_{lin}$, with the wavenumber k. This initial velocity shear v_{lin} corresponds to the linear growth rate in RMI[23,36]

$$v_{lin}=\frac{\rho_1\delta v_1^*-\rho_2\delta v_2^*}{\rho_1+\rho_2}, \quad (2)$$

in which $\delta v_{1,2}^*$ represents the transverse velocities immediately after the shock-interface interaction in RMI.[23,26,36] The length and time are normalized by the wavenumber k and the initial shear velocity v_{lin} such as kx, ky, and $kv_{lin}t$.

The effects of compressibility are important in RMI when an incident shock is strong and the transmitted and reflected shocks are very close to the interface, i.e., in the earlier stage of the RMI growth.[36,53,54] Therefore, the linear growth rate depends on the compressibility. A strong incident shock leaves large bulk vortices behind the transmitted and reflected rippled shocks, and the large bulk vortices suppress the linear growth of RMI because the flow near the interface generated by the bulk vortices is opposite to the flow caused by the interface vorticity.[34,36] This phenomenon motivates our present work. However, as the shocks separate from the interface, the perturbations of the pressure and density behind the rippled shocks will

decay in time.[36,55] Then asymptotically, the perturbations become incompressible independent of the incident shock intensity. Therefore, we restrict ourselves here to the incompressible flows for the nonlinear interaction between a nonuniform vortex sheet and bulk vortices. The vortex sheet model was validated by comparing its nonlinear interface dynamics with the shocked interface with the use of two-dimensional hydrodynamic simulations.[24] The effect of the compressibility can be incorporated into the linear growth rate by using the full expression of that of which concrete formula is given by, e.g., Eq. (3) in Ref. 28 for a case that a shock is reflected or Eq. (3) in Ref. 56 for a case that a rarefaction wave is reflected, instead of Eq. (1) in the present paper.

We parameterize points on the interface $\boldsymbol{x} = \boldsymbol{X}$ as

$$\boldsymbol{X}(e,t) = [X(e,t), Y(e,t)],$$

using a Lagrangian parameter e ($-\pi \le e \le \pi$). Now we assume the periodicity in the x direction. When bulk vortices exist in the system, the vortex induced fluid velocity $\boldsymbol{W}$ at an arbitrary point $\boldsymbol{x} = (x, y)$ is given as the sum of the two velocities

$$\boldsymbol{W} = \boldsymbol{W}_s + \boldsymbol{W}_p, \tag{3}$$

in which $\boldsymbol{W}_s = (W_{s,x}, W_{s,y})$ is the velocity by the contribution from the interface

$$\begin{aligned} W_{s,x}(x,y) &= -\frac{1}{4\pi}\int_{-\pi}^{\pi} \frac{\gamma(e',t)s_e(e',t)\sinh(y - Y(e',t))}{\cosh(y - Y(e',t)) - \cos(x - X(e',t))}de', \\ W_{s,y}(x,y) &= \frac{1}{4\pi}\int_{-\pi}^{\pi} \frac{\gamma(e',t)s_e(e',t)\sin(x - X(e',t))}{\cosh(y - Y(e',t)) - \cos(x - X(e',t))}de', \end{aligned} \tag{4}$$

where $\boldsymbol{\gamma} = \boldsymbol{u}_1 - \boldsymbol{u}_2$, and $\gamma = \boldsymbol{\gamma}\cdot\boldsymbol{t} = \partial\Gamma/\partial s$ denotes the (true) vortex sheet strength derived from the circulation $\Gamma \equiv \phi_1 - \phi_2$, in which s is the arc length and $\boldsymbol{t}$ is the unit tangential vector of the interface, respectively. Here, the subscript e denotes the differentiation with respect to e and $s_e = \sqrt{X_e^2 + Y_e^2}$. We take the principal value of the integral (4) when the point (x, y) is on the interface: $(x, y) = (X, Y)$. Equation (4) is called the Birkhoff–Rott equation[57–59] if (x, y) is on the interface and it provides the velocity of a vortex sheet.

On the other hand, $\boldsymbol{W}_p = (W_{p,x}, W_{p,y})$ is the velocity by the contribution from bulk vortices given by

$$\begin{aligned} W_{p,x}(x,y) &= -\frac{1}{4\pi}\sum_{j=1}^{N} \frac{\gamma_{p,j}\sinh(y - y_{p,j}(t))}{\cosh(y - y_{p,j}(t)) - \cos(x - x_{p,j}(t))}, \\ W_{p,y}(x,y) &= \frac{1}{4\pi}\sum_{j=1}^{N} \frac{\gamma_{p,j}\sin(x - x_{p,j}(k))}{\cosh(y - y_{p,j}(t)) - \cos(x - x_{p,j}(t))}, \end{aligned} \tag{5}$$

where $\gamma_{p,j}$ and N denote the strength of point vortex j and the number of point vortices, respectively. Here, although the point vortex has measure zero from its definition, we have defined its strength using the wavelength of the initial sinusoidal vortex sheet following Cummings.[6] Namely, the strength of point vortex j is defined as $\gamma_{p,j} = \Gamma_{p,j}/\lambda$, where $\Gamma_{p,j}$ is the circulation of point vortex j and $\lambda\,(= 2\pi)$ is the normalized wavelength of the initial perturbation of the vortex sheet. Traditionally, the circulation $\Gamma_{p,j}$ is called the strength of point vortex j.[48]

We define the interfacial velocity $\boldsymbol{u}^+$ of a Lagrangian point labeled by e as

$$\boldsymbol{u}^+(e,t) = \boldsymbol{W}|_{\boldsymbol{x}=\boldsymbol{X}} + \frac{\tilde{\alpha}\gamma}{2}\boldsymbol{t}, \tag{6}$$

where $\boldsymbol{W}|_{\boldsymbol{x}=\boldsymbol{X}} \equiv (U, V)$ corresponds to the average velocity $(\boldsymbol{u}_1 + \boldsymbol{u}_2)/2$ at the interface and $\tilde{\alpha}$ is an artificial parameter depending on the Atwood number A. There is arbitrariness on how to select the tangential velocity of the interface, and the parameter $\tilde{\alpha}$ controls the magnitude of the tangential velocity. This parameter was first introduced by Pullin.[60] When we choose $\tilde{\alpha} = A$, the tangential component of the interfacial velocity $\boldsymbol{u}^+$ becomes a weighted average velocity of two fluids

$$\boldsymbol{u}^+ = \frac{\rho_1\boldsymbol{u}_1 + \rho_2\boldsymbol{u}_2}{\rho_1 + \rho_2}.$$

Sometimes, the large value of A causes clustering of the Lagrange points in the neighborhood of vortex cores, by which the computation breaks down. To avoid this and perform long time computations, larger $\tilde{\alpha}$ than $\tilde{\alpha} = A$ is often selected.

Equating $\boldsymbol{u}^+$ with the evolution of the interface,[61] we have the interfacial velocity for the Lagrangian motion as

$$\frac{\mathrm{d}\boldsymbol{X}}{\mathrm{d}t} = \boldsymbol{W}|_{\boldsymbol{x}=\boldsymbol{X}} + \frac{\tilde{\alpha}\gamma}{2}\boldsymbol{t}, \tag{7}$$

where

$$\frac{\mathrm{d}}{\mathrm{d}t} = \frac{\partial}{\partial t} + \boldsymbol{u}^+\cdot\nabla,$$

is the Lagrangian derivative in the frame moving with the interface.

A point vortex velocity is given by substituting its location $\boldsymbol{x} = \boldsymbol{x}_{p,i}$ into (3)

$$\frac{dx_{p,i}}{dt} = W_s|_{x=x_{p,i}} + W_p|_{x=x_{p,i}}\,(i = 1, 2, \ldots, N), \tag{8}$$

where the term of $j = i$ (own contribution) in the integral (5) is excluded from the summation.

Using the relation $\Gamma = \phi_1 - \phi_2$, we rewrite Eq. (1) as

$$\frac{\mathrm{d}\Gamma}{\mathrm{d}t} = 2A\frac{\mathrm{d}\Phi}{\mathrm{d}t} - A\boldsymbol{W}\cdot\boldsymbol{W} + \frac{A + 2\tilde{\alpha}}{4}\boldsymbol{\gamma}\cdot\boldsymbol{\gamma} - \tilde{\alpha}A\boldsymbol{\gamma}\cdot\boldsymbol{W}, \tag{9}$$

where $\Phi = (\phi_1 + \phi_2)/2$. Differentiating (9) with respect to e, we obtain the following Fredholm integral equation of the second kind

$$\begin{aligned} \frac{\mathrm{d}\gamma}{\mathrm{d}t} = \frac{2A}{s_e}\left(X_e\frac{\mathrm{d}U}{\mathrm{d}t} + Y_e\frac{\mathrm{d}V}{\mathrm{d}t}\right) \\ - \frac{(1 + \tilde{\alpha}A)\gamma}{s_e^2}(X_eU_e + Y_eV_e) + \frac{A + \tilde{\alpha}}{4s_e}(\gamma^2)_e. \end{aligned} \tag{10}$$

Solving Eqs. (7), (8), and (10) simultaneously by taking into account Eqs. (4) and (5), we can determine the motion of the interface and bulk point vortices, including whole velocity field.

Here, we mention the extension of the present model to MHD flows. A theoretical model[15] has been proposed to describe fully nonlinear dynamics of interfaces in two-dimensional MHD flows based on an idea of the nonuniform current-vortex sheet. The extension of the present model is possible in a similar way by introducing point current-vortices (point vortices with line-current) that correspond to point vortices in pure hydrodynamic flows, and by assuming the

current and vorticity free conditions at $t=0$ in the bulk except the singular points, $\boldsymbol{x}_{p,i}$ $(i=1,2,\ldots)$, where point current-vortices exist. Unlike neutral gasses, the vorticity and the line-current density of the point vortices are not conserved in MHD flows; therefore, we need to calculate the temporal evolution of both the strength of point vortices and the strength of line current together with the vortex sheet strength and the current sheet strength of the interface. Details of the extension to MHD flows are beyond the scope of this paper, and we will present elsewhere.

III. NUMERICAL RESULTS

In numerical calculations, all physical quantities are normalized by the wavenumber k and the initial velocity shear of the vortex sheet v_{lin} given by Eq. (2) so that they are dimensionless. From now on, the dimensionless variables space $k\boldsymbol{x}$, time $kv_{lin}t$, circulation of vortex sheet $k\Gamma/v_{lin}$, vortex sheet strength γ/v_{lin}, circulation of point vortex j $k\Gamma_{p,j}/v_{lin}$, and strength of point vortex $\gamma_{p,j}/v_{lin}$ $(j=1,2,\ldots,N)$ are used as $\boldsymbol{x}$, t, Γ, γ, $\Gamma_{p,j}$, and $\gamma_{p,j}$ $(j=1,2,\ldots,N)$. In general, RMI velocity shear at the corrugated interface and bulk vortices depends on the strength of an incident shock, the initial density ratio of two fluids, a corrugation amplitude of an interface, and thermodynamic properties of the fluids. However, in our model, the fluid velocity is normalized by the initial velocity shear at the interface induced by RMI, which is equivalent to the linear growth rate of RMI. Therefore, the dependence of the velocity on such initial conditions does not appear explicitly in the model.

We fix the Atwood number A as $A=-0.2$ $(\rho_2<\rho_1)$ throughout this section. Here, we select the artificial parameter $\tilde{\alpha}$ in Eqs. (6), (7), and (10) as $\tilde{\alpha}=A^2$. This value was first selected by Kerr[62] for long time computations of vortex sheets with finite Atwood numbers. The regularized parameter δ in Eq. (A1) is chosen as $\delta=0.15$.[43] Krasny[42] investigated δ dependence of the results in detail and concluded that an appropriate value of δ is in the range $\delta=0.1\sim0.2$. The value $\delta=0.15$ is adopted so as to be best suited for experiments by Matsuoka and Nishihara[43] and Jacobs and Sheeley[63] and the results by the hydrodynamic simulations[24] and the magnetohydrodynamic simulations.[15] When we select $\delta=0.2$, the roll-up of the vortex sheet becomes considerably weak but there is not much of a difference in the results between $\delta=0.1$ and $\delta=0.15$.[43]

The threshold value $d_{\rm lim}$ in Eq. (A4) is selected as $d_{\rm lim}=0.125$ throughout the calculations in this section. This value is chosen as about five times larger than the initial average interval of the Lagrangian points ($2\pi/N$, $N=256$ the number of initial grid points). If we select smaller d_{lim}, the computational time becomes very long to obtain the same results, and if we select larger d_{lim}, we cannot obtain sufficient spatial resolution. For details on the numerical schemes adopted here, refer to the Appendix.

A. Interfacial dynamics of the Richtmyer–Meshkov instability without point vortices

In this subsection, we provide the interfacial dynamics of single-mode pure RMI without point vortices for reference to subsequent discussions. Since RMI is essentially driven by the nonuniform velocity shear left by the transmitted and reflected shocks at the interface,[26,36] we consider here a sinusoidal velocity shear at the interface without spatial perturbation as an initial condition. Under the above normalizations, the initial condition of the interface is given as follows:[43]

$$\begin{aligned} x(e,0)&=e, \quad (-\pi\le e\le\pi),\\ y(e,0)&=0,\\ \gamma(e,0)&=-2\sin e, \end{aligned} \tag{11}$$

where the factor –2 in $\gamma(e,0)$ is due to the normalization of the maximum difference of the tangential velocity of the vortex sheet at $e=\pm\pi/2$.

Figure 1 shows the velocity field and the interfacial structure of single-mode RMI without point vortices, where the velocity field is calculated by Eq. (3). As given by the initial condition (11), the vortex sheet strength is positive in $x<0$ ($\gamma=2$ at $x=-\pi/2$), while it is negative in $x>0$ ($\gamma=-2$ at $x=\pi/2$). The spike that grows on RMI eventually forms a mushroom and the tips of the mushroom umbrella roll up with time.[43,63] The vortex sheet strength γ at time $t=5$ takes its maximum value (in absolute value) at the center of the mushroom umbrella, which we refer to the vortex cores[52] here. For the initial condition (11), the vortex cores always appear in the neighborhood of $x=\pm\pi/2$ $(e=\pm\pi/2)$, in which the vortex sheet strength with positive sign (counterclockwise rotation) appears at the left core $(x\sim-\pi/2)$, while the sheet strength with negative sign (clockwise rotation) appears at the right core $(x\sim\pi/2)$.

The interfacial structure at the fully nonlinear stage ($t=12.176$) is presented in Fig. 2, where the number of grid points N increases from $N=256$ ($t=0$) to $N=1030$ ($t=12.176$) per wavelength. In the figure, a period of two wavelengths ($\lambda=2\pi$) is depicted. It should be noted that the number of mushrooms, which corresponds to the number of bubbles and spikes, is only one in a period for this single-mode initial condition. Similar interfacial structures were experimentally observed by Jacobs and Sheeley.[63] We compare the results shown in Figs. 1 and 2 to the vortex sheet dynamics with bulk point vortices in Subsection III B.

B. Interaction between the vortex sheet and bulk point vortices

In this subsection, we consider the nonlinear interaction of the nonuniform vortex sheet with bulk point vortices. For example, in ICF[37,38] multi-shocks propagating through a nonuniform multi-layer target may leave bulk vortices behind the shocks, and nonuniform interfaces that are unstable for RMI may interact with these bulk vortices. It is also well known even in linear RMI that the interaction of an

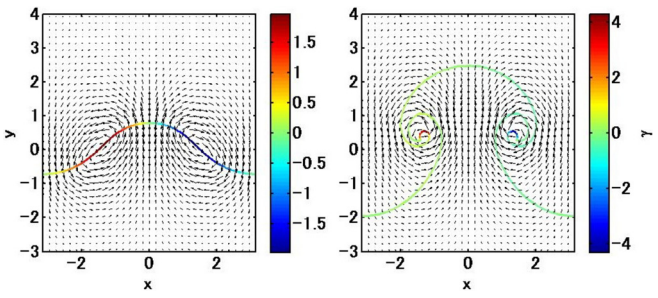

FIG. 1. Interfacial structures with the colored scale of the vortex sheet strength γ and the velocity fields with the initial condition given by Eq. (11), where the arrows indicate velocity fields; left figure at the early stage ($t=1$) and the right one at the fully nonlinear stage ($t=5$), respectively.

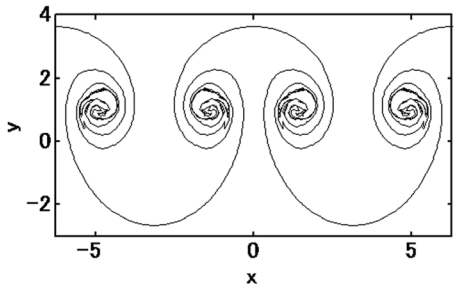

FIG. 2. Interfacial structure at $t = 12.176$, where the final grid number $N = 1030$ per wavelength. A period of two wavelengths is depicted in the figure.

incident shock with a corrugated interface induces ripples on the shock fronts of both the transmitted and reflected shock waves. Also, due to the conservation of tangential velocity at the rippled shock fronts, transverse velocity perturbations are generated inside the compressed fluids, which account for vorticity generation in the bulks.[10,28,33,34,36] In the present work, we assume that the bulk vortices are given by point vortices for simplicity. The spatial distribution of the bulk vortices was clearly visualized, for instance, in Fig. 3 of Cobos-Campos and Wouchuk.[34] For our initial conditions (11), where the normalized sheet strength γ has a maximum (positive) value at $x = -\pi/2$ and a minimum (negative) value at $x = \pi/2$, the positions of the bulk vortices approximately correspond to $x \sim \pm\pi/2$ and $y \sim \pi, 3\pi, \cdots$, and $-\pi/5, -4\pi/5, \cdots$, in which the positive and negative vortices appear alternately in the y direction.[34,35]

Here, for simplicity, we set the initial distribution of four and eight point vortices close to the vortex sheet so that two (four) point vortices are placed over the vortex sheet and the other two (four) vortices under the sheet for the case of four (eight) vortices. The configuration of point vortices and their signs are related to the linear RMI discussed above. Case 1 and Case 4 below correspond to the

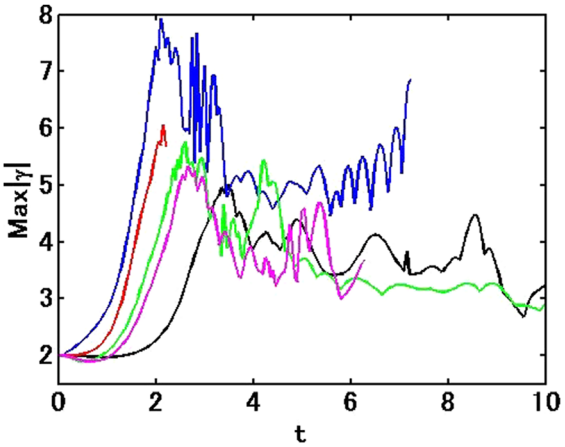

FIG. 3. Temporal evolution of the absolute value of the maximum sheet strength γ. Initial condition (11) (black line), Case 1 [initial conditions defined by Eq. (14), green line], Case 2 [initial conditions defined by Eq. (15), blue line], Case 3 [initial conditions defined by Eq. (16), red line], and Case 4 [initial conditions defined by Eq. (17), pink line].

configuration obtained by the linear analysis of Cobos-Campos and Wouchuk.[34,35] Case 2 and Case 3 are adopted to compare with those cases, which are possible locations in experiments of ICF.

The initial position of the four-vortex problem is given as

$$\begin{aligned} &x_{p,1}(0) = -\frac{\pi}{2}, \quad y_{p,1}(0) = \frac{\pi}{4}, \quad \gamma_{p,1}(0) = \gamma_1, \\ &x_{p,2}(0) = -\frac{\pi}{2}, \quad y_{p,2}(0) = -\frac{\pi}{4}, \quad \gamma_{p,2}(0) = \gamma_2, \\ &x_{p,3}(0) = \frac{\pi}{2}, \quad y_{p,3}(0) = \frac{\pi}{4}, \quad \gamma_{p,3}(0) = \gamma_3, \\ &x_{p,4}(0) = \frac{\pi}{2}, \quad y_{p,4}(0) = -\frac{\pi}{4}, \quad \gamma_{p,4}(0) = \gamma_4. \end{aligned} \tag{12}$$

For the eight-vortex problem, we set the initial position of four point vortices from $(p, 1)$ to $(p, 4)$, which are closer to the vortex sheet, as the same as Eq. (12), and the other four vortices from $(p, 5)$ to $(p, 8)$, which are outside of the above four vortices, are set to be

$$\begin{aligned} &x_{p,5}(0) = -\frac{\pi}{2}, \quad y_{p,5}(0) = \frac{\pi}{2}, \quad \gamma_{p,5}(0) = \gamma_5, \\ &x_{p,6}(0) = -\frac{\pi}{2}, \quad y_{p,6}(0) = -\frac{\pi}{2}, \quad \gamma_{p,6}(0) = \gamma_6, \\ &x_{p,7}(0) = \frac{\pi}{2}, \quad y_{p,7}(0) = \frac{\pi}{2}, \quad \gamma_{p,7}(0) = \gamma_7, \\ &x_{p,8}(0) = \frac{\pi}{2}, \quad y_{p,8}(0) = -\frac{\pi}{2}, \quad \gamma_{p,8}(0) = \gamma_8. \end{aligned} \tag{13}$$

Here, we consider the following four initial distributions for the strength of point vortices. The oscillating rippled shocks generate bulk vortices with the opposite sign of the sheet strength on the interface within their first period of oscillation, which corresponds to the first one (Case 1, four-vortex problem) given by

$$\gamma_1 = \gamma_2 = -\gamma_0, \quad \gamma_3 = \gamma_4 = \gamma_0. \tag{14}$$

It may be interesting to investigate the interface dynamics with different configuration of the point vortices and interface velocity shear such as (Case 2, four-vortex problem)

$$\gamma_1 = \gamma_4 = \gamma_0, \quad \gamma_2 = \gamma_3 = -\gamma_0, \tag{15}$$

and (Case 3, four-vortex problem)

$$\gamma_1 = \gamma_2 = \gamma_0, \quad \gamma_3 = \gamma_4 = -\gamma_0. \tag{16}$$

In Case 2, there are point vortices with different signs across the interface. In Case 3, the signs of the sheet strength and the normalized point vortex strength are the same, and they are located in one side, in which they have positive values in $x < 0$ and negative values in $x > 0$. These three cases result in quite different dynamics of the point vortices and interfacial structure as will be shown later. The last case is (Case 4, eight-vortex problem)

$$\gamma_5 = \gamma_6 = \gamma_0, \quad \gamma_7 = \gamma_8 = -\gamma_0. \tag{17}$$

For Case 4, the strengths from γ_1 to γ_4 are the same as those in (14), Case 1. Here, we fix the initial strength γ_0 as $\gamma_0 = 1$. This point vortex strength is half the initial vortex sheet strength given by Eq. (11). The position of the point vortex and the sign of the strength in Case 4 are the closest one in the linear RMI.[34] The oscillating rippled shocks decay as they propagate away from the interface[36] and therefore, the vorticity of bulk vortices also decreases as the distance from

the interface becomes large.[34,35] However, we set them to the same value for simplicity in the current study.

In the initial condition given by Eq. (14) (Case 1), the point vortices are set so that the sign of the point vortices is opposite to that of the vortex core of the sheet (two vortices at $x = -\pi/2$ are negative sign and two vortices at $x = \pi/2$ are positive sign). On the other hand, the initial condition (15) (Case 2) corresponds to the case that the strength of the point vortices locating over the vortex sheet is opposite to the condition (14). In the initial condition (16) (Case 3), the sign of the point vortices is the same as the core of the sheet (two vortices at $x = -\pi/2$ are positive sign and two vortices at $x = \pi/2$ are negative sign). In the initial condition given by Eq. (17) (Case 4), the strength of the four point vortices closer to the vortex sheet is the same as the one in Case 1, while the location of the other four point vortices far from the vortex sheet is the same as the one in Case 3.

We present the temporal evolution of the absolute value of the maximum sheet strength Max $|\gamma|$ in Fig. 3. The figure shows that the vortex sheet strength with point vortices grows much faster and becomes much larger than that without point vortices (black line) in the nonlinear stage. The nonlinear interaction of point vortices with a nonuniform vortex sheet generally increases the strength of the sheet, and its maximum values depend on the signs of the strengths of point vortices. We discuss this for each case below.

1. Motion of the vortex sheet and point vortices with the strength of the opposite sign to the vortex cores (Case 1)

When the bulk point vortices are set to the opposite sign of the sheet strength [refer to the initial condition (14)], the point vortices induce the velocity shear on the sheet so that the sheet strength is enhanced as the point vortices approach the sheet. The rapid increase in the sheet strength was seen at around time $t = 2$, shown by the green line in Fig. 3. As a result, the point vortex forms a new vortex core with the increased sheet strength and a new type of the vortex pair, and a new (satellite) mushroom is created. Figure 4 shows this process. The blue (red) point vortices approach the vortex sheet with red (blue) color while rotating ($t = 1$) and form new vortex cores with strong sheet strengths, in which process, the vortex sheet with strong sheet strength splits into four cores (two in the neighborhood of spike and the other two in the neighborhood of bubbles). These vortex cores make pseudo-vortex pairs with those point vortices, and new mushrooms of which number coinciding with that of point vortices appear on the sheet ($t = 3 - 5$). The pseudo-vortex pair consists of a point vortex and a sheet vortex core although their strengths are not the same in magnitude.

As seen in the right figure of Fig. 5, when the vortex sheet is absent, the point vortex pairs with the same sign rotate. Since the vortex pairs are not isolated, the rotation of point vortices is not a perfect circle but slightly elongated in the y-direction. On the other hand, when the nonuniform vortex sheet exists, the vortices are forced to rotate in the opposite direction to that of the right figure due to RMI flow as depicted in the left figure of Fig. 5 (also refer to the direction of the velocity field in Fig. 4, $t = 1 - 3$) for the initial conditions given by Eqs. (11) and (14). Namely, the velocity of the background fluid where there are point vortices is larger than the rotation velocity induced by the vortex pairs. Moreover, when a point vortex approaches the vortex sheet, the point vortex forms a pseudo-vortex pair with the vortex core of the opposite sign, not with another point vortex, as described above.

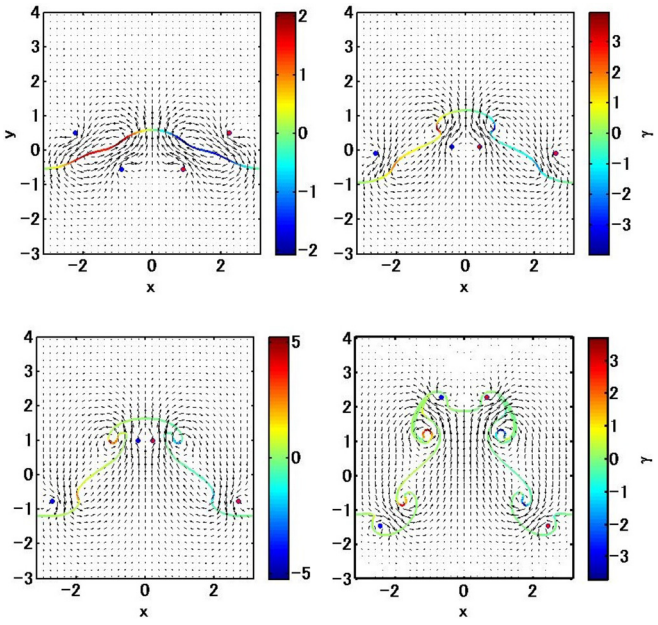

FIG. 4. Interfacial structures with the colored scale of the vortex sheet strength and the velocity fields with the initial condition given by Eq. (14), where the upper left and right figures show $t = 1$ and $t = 2$, and the lower left and right $t = 3$ and $t = 5$, respectively. The red and blue points denote the strength of point vortices having positive ($\gamma_0 = 1$, counterclockwise rotation) and negative ($\gamma_0 = -1$, clockwise rotation) signs, respectively.

In order to make the positions of the newly created bubbles and spikes clearer, we show the interfacial structure at the final stage ($t = 10.7765$) over two periods in Fig. 6, where the number of grid points N increases from $N = 256$ ($t = 0$) to $N = 1784$ ($t = 10.7765$) per wavelength. We see that the interfacial structure becomes extremely convoluted due to the presence of point vortices compared to that without point vortices (refer to Fig. 2). It should be noted that there

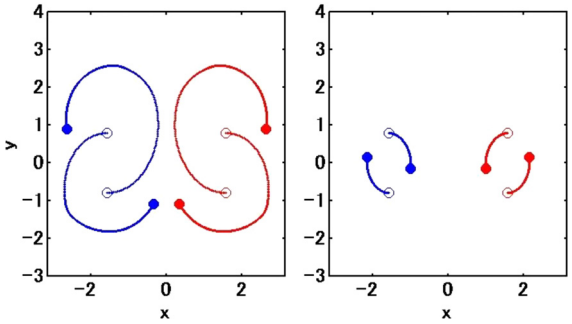

FIG. 5. Loci of point vortices with the nonuniform vortex sheet (left) and without the vortex sheet for the initial condition (14) (right), where the colors are the same as those in Fig. 4, and both figures take the same period of time ($0 \leq t \leq 10.7765$). The markers of a white circle and filled circle denote the initial and final positions of point vortices, respectively.

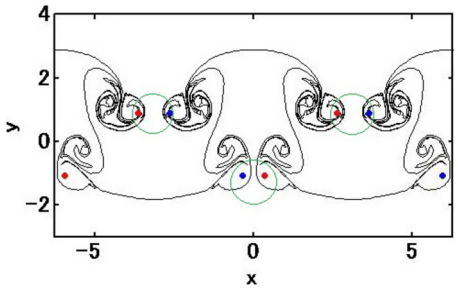

FIG. 6. Interfacial structure at $t = 10.7765$, where the final grid number $N = 1784$ per wavelength. A period of two wavelengths is depicted in the figure.

are five mushrooms created (four satellite mushrooms created by the point vortices stated above and one large mushroom originally exists due to RMI). We can see the number of bubbles and spikes generated in one period in this figure. The point vortices in the region of $y < 0$ in Fig. 6 were initially located in the lighter fluid. A bubble of light fluid surrounding the point vortex enters a region of heavier fluid, where the bubble region forms a mushroom shape. On the other hand, a spike of heavy fluid surrounding the point vortex in the region of $y > 0$ enters a region of lighter fluid forming mushroom spike with heavier fluid as seen in the conventional RMI.

It is interesting to note that two new pairs of the point vortices might be formed at this time, the first pairs are in the neighborhood of $x = 0, \pm 2\pi$ and $y = -1$, and the other pairs are in the neighborhood of $x = \pm\pi$ and $y = 1$. We denote a part (the ones in the neighborhood of $x = 0$, $y = -1$ and $x = \pm\pi$, $y = 1$) of those as thin green circles in Fig. 6. The vortices in the former pairs are initially in the lighter fluid, i.e., above the interface, while the vortices in the latter pairs are initially in the heavier fluid, i.e., below the interface. The latter pairs created in the neighborhood of $y = 1$ are due to the periodic boundary condition of the system employed.

2. Motion of the vortex sheet and point vortices with different signs between the vortex cores (Case 2)

Figure 7 shows the interfacial structures, giving the velocity field and the color scaled velocity shear along the interface at $t = 1, 2, 3,$ and 5 for the initial condition (15), in which the signs of the point vortices over the sheet (the lighter fluid) are opposite to those in the initial condition (14) (refer to the figures $t = 1$ in Figs. 4 and 7). In this case, two vortices, $(p, 1)$ and $(p, 2)$ [or $(p, 3)$ and $(p, 4)$] form a pair, which move almost parallel to the x axis in the absence of the vortex sheet, at least up to the time $t \sim 7$, as shown in the right panel of Fig. 8. The motion of two point vortices $(p, 2)$ and $(p, 4)$ in the heavier fluid at the early stage is the same as its background fluid motion due to RMI. Therefore, their distance becomes closer, and they form a new pair and go upwards with the heavier fluid.

Since the sign of these point vortices $(p, 2)$ and $(p, 4)$ (in the heavier fluid) is opposite to that of the velocity shear on the sheet, these vortices make the pseudo-vortex pairs with the vortex cores on the sheet ($t = 2$) approach the sheet, and two local mushrooms are created on both sides of the spike of the original mushroom by RMI ($t = 2 - 5$ in Fig. 7). The other two point vortices $(p, 1)$ and $(p, 3)$ initially located over the sheet move downwards with the background

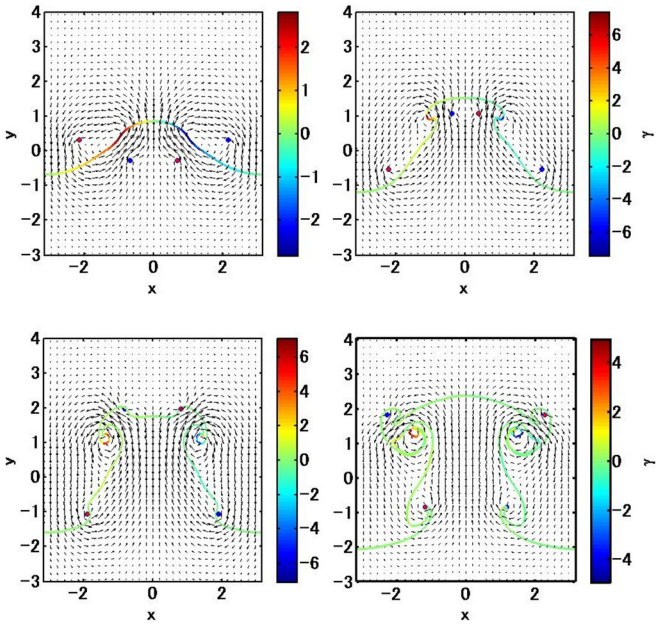

FIG. 7. Interfacial structures with the colored scale of the vortex sheet strength and the velocity fields with the initial condition given by Eq. (15), where the upper left and right figures show $t = 1$ and $t = 2$, and the lower left and right $t = 3$ and $t = 5$, respectively. The colors of point vortices are the same as those in Fig. 4.

lighter fluid separating each other as shown in Figs. 7 and 8. Even when the vortices get close to the sheet, they do not induce vortex cores because they have the same signs with the velocity shear on the sheet. For this case, the point vortices and the sheet begin to rotate (as found in the case of Subsection III B 3). As a result, the lighter fluid with these vortices penetrates the heavier fluid as seen at $t = 5$ in Fig. 7.

Three mushrooms are finally formed (the original large mushroom and two satellite mushrooms created on both sides of the spike of the original mushroom) for the initial condition (15). It should be noted that the maximum strength of the vortex sheet Max $|\gamma|$ is larger than other two cases of Case 1 and Case 3 as shown by the blue line in Fig. 3. When $t \geq 3$, all of the point vortices seem to be trapped in or on the interface, and they stay in the neighborhood of the vortex sheet

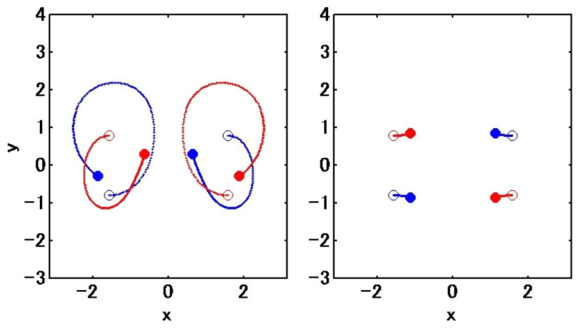

FIG. 8. Loci of point vortices for the initial condition (15), where the colors, and markers of the initial and final positions are the same as those in Fig. 5. Two figures take the same period of time ($0 \leq t \leq 7.23$).

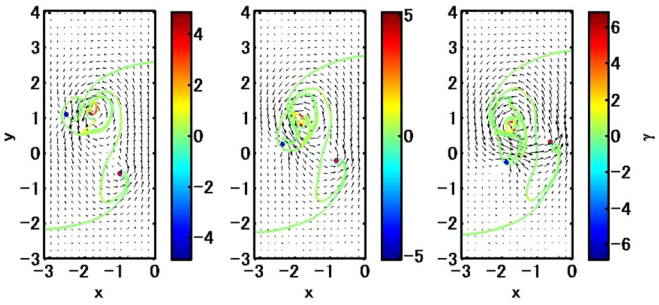

FIG. 9. Interfacial structures with the colored scale of the vortex sheet strength and the velocity fields with the initial condition (15) in the region $-\pi \le x \le 0$ at fully nonlinear stage, where the left, middle, and right figures show $t = 5.73$ (grid number $N = 546$), $t = 6.48$ ($N = 708$), and $t = 7.23$ ($N = 886$), respectively.

for a relatively long time as found in Figs. 7 and 9. This indicates that the normal velocity of the point vortices coincides with that of the vortex sheet as they approach the sheet.

3. Motion of the vortex sheet and point vortices with the strength of the same sign to the vortex cores (Case 3)

We show the interfacial structures with the colored scale of the vortex sheet strength and the velocity fields at $t = 1$ and 2 in Fig. 10 for the case that the initial point vortices are set with the same signs as the vortex sheet strength [refer to the initial condition (16)]. The direction of the rotation of the point vortices in the absence of the vortex sheet is the opposite of that in Case 1, and it is also the same as that of the background fluid motion due to RMI. Two point vortices $(p, 2)$ and $(p, 4)$ in Eq. (12) under the sheet (the side of heavier fluid) at $t = 0$ are then accelerated upwards by the flow of RMI, while two point vortices $(p, 1)$ and $(p, 3)$ in Eq. (12) over the sheet at $t = 0$ are accelerated downwards. It should also be noted that the distance between the point vortices $(p, 2)$ and $(p, 4)$ becomes smaller, and they become a new vortex pair. As a result, their upward movement is further accelerated. The other new pair of $(p, 1)$ and $(p, 3)$ formed due to the periodic boundary condition is accelerated to downwards. This situation is found in the orbits of point vortices in Fig. 11, where the point vortices without the interface (right figure) hardly move in this period of time.

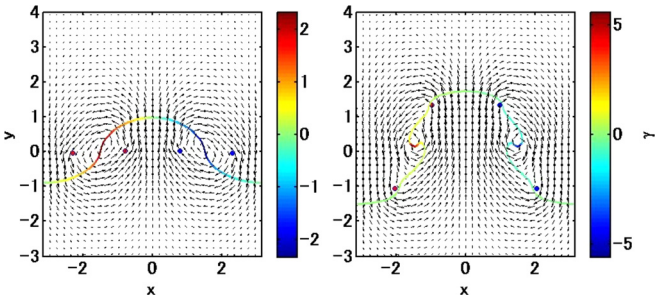

FIG. 10. Interfacial structures with the colored scale of the vortex sheet strength and the velocity fields with the initial condition given by Eq. (16), where the left and right figures show $t = 1$ and $t = 2$, respectively. The colors of point vortices are the same as those in Figs. 4 and 7.

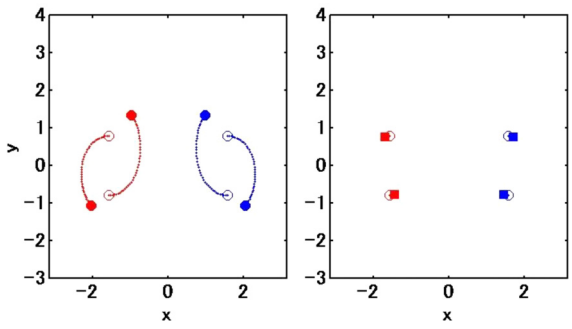

FIG. 11. Loci of point vortices for the initial condition (16), where the colors, and markers of the initial and final positions are the same as those in Figs. 5 and 8. Two figures take the same period of time ($0 \le t \le 2$).

When $t > 2$, the bulk velocity induced by RMI, pulling sideways the vortex pair, becomes larger than the velocity that the pair moves upwards; therefore, the two vortices $(p, 2)$ and $(p, 4)$ are forced to separate, and finally, they reach the interface and cross it. At around this time, the other pair of $(p, 1)$ and $(p, 3)$, which are initially located over the sheet (the side of lighter fluid), also reaches the interface. However, as we see from Eqs. (7) and (8), the normal velocity of the point vortices coincides with that of the vortex sheet at the interface when the sheet is parameterized with a continuous variable; namely, the point vortices cannot cross the interface. We can continue to calculate for $t > 2$ as well as Case 1 and Case 2; however, the result that the point vortices cross the interface is inconsistent with the immiscible condition adopted here. Therefore, we abort the computation at $t = 2$ for Case 3.

4. Interaction of the vortex sheet and eight point vortices (Case 4)

Figure 12 shows the interfacial structures with the colored scale of the vortex sheet strength and the velocity fields at $t = 1$, 2, 3, and 5 for the initial condition (17). Since the initial location of the four point vortices closer to the vortex sheet is the same as the one in Case 1, the motion of both the point vortices and the vortex sheet is very similar to that found in Fig. 4 in the early nonlinear stage ($1 \le t \le 2$), in which these four vortices make the pseudo-vortex pairs with the vortex cores. Since the four vortices initially located outside of the above four vortices have the same signs as their neighboring cores initially, they rotate the satellite mushrooms as also found in Fig. 13. The maximum sheet strength Max $|\gamma|$ (refer to the pink line of Fig. 3) appears at the core of the satellite mushrooms on either side of the original spike, where these cores make the pseudo-pairs with the point vortices originally located in the heavier (under the sheet) fluid. The point vortices forming the pseudo-vortex pairs in the region of $y > 0$ at $t = 5$ in Fig. 12 are accelerated downwards due to RMI flow and the presence of the point vortices with the same signs as the vortex cores, while the point vortices originally located in the lighter (over the sheet) fluid make an incomplete pseudo-pair with the lower weak vortex cores at $t = 5$.

Figure 14 shows the loci of point vortices with the initial condition (17). The motion described above is depicted in the left figure of Fig. 14. The two point vortices initially located far from the sheet in

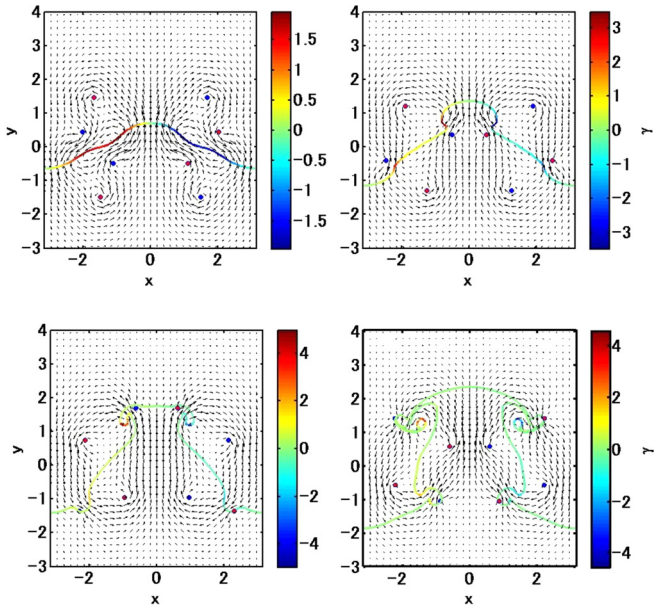

FIG. 12. Interfacial structures with the colored scale of the vortex sheet strength and the velocity fields with the initial condition given by Eqs. (13) and (17), where the upper left and right figures show $t=1$ and $t=2$, and the lower left and right $t=3$ and $t=5$, respectively. The colors of point vortices are the same as those in Figs. 4, 7, and 10.

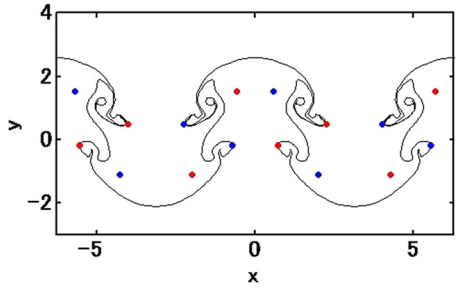

FIG. 13. Interfacial structure at $t=6$, where the final grid number $N=508$ per wavelength. A period of two wavelengths is depicted in the figure.

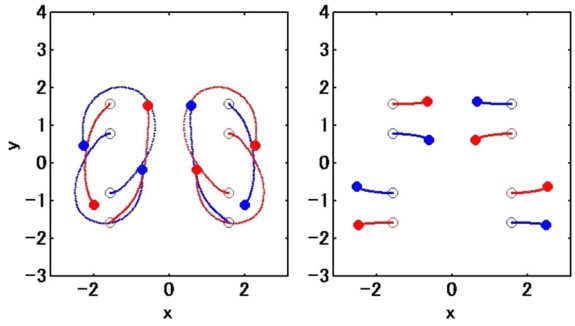

FIG. 14. Loci of point vortices for the initial condition (17), where the colors, and markers of the initial and final positions are the same as those in Figs. 5, 8, and 11. Two figures take the same period of time ($0 \le t \le 6$).

the heavier fluid $[(p,6)$ and $(p,8)]$ form a vortex pair with the two vortices initially located closer to the sheet in the lighter fluid $[(p,1)$ and $(p,3)]$ in the neighborhood of the original spike. On the other hand, the two point vortices initially located far from the sheet in the lighter fluid $[(p,5)$ and $(p,7)]$ form a vortex pair with the two vortices initially located closer to the sheet in the heavier fluid $[(p,2)$ and $(p,4)]$ in the neighborhood of the original bubble. This vortex pair moves downwards as found at $t=5$ in Figs. 12 and 13. The exchange of the vortex pair is caused by the fact that a point vortex in the original pair is trapped in the neighborhood of the interface to form the pseudo-vortex pairs. This kind of exchange is not found in the motion of a small number of vortices, such as the four-vortex problem described in Subsections III B 1–III B 3.

IV. CONCLUSION AND DISCUSSIONS

We have developed a theoretical model to describe the nonlinear interaction of a nonuniform vortex sheet with bulk point vortices, taking RMI as an example. Our model and numerical method can capture the complicated behavior of the vortex sheet and point vortices, including the fluid motion in bulk. We found that motion of a vortex sheet coexisting with point vortices is extremely different from that without point vortices. This indicates that the motion of a vortex sheet is unstable for an external field such as the motion of point vortices.

The strength of the vortex sheet increases faster and becomes larger than that of pure RMI without point vortices as the point vortices approach the sheet. A point vortex approaching a nonuniform vortex sheet induces a vortex core on the sheet and forms a pseudo-vortex pair with that core, only if the strength of the point vortex has the opposite sign of the local sheet strength and is large enough. In a pseudo-vortex pair, the strength of a point vortex and the sheet strength of a vortex core is not the same in magnitude. The pseudo-vortex pair generates a local satellite mushroom profile on the interface. It is also observed that bubbles of lighter fluid surrounding point vortices enter the region of heavier fluid forming mushroom-shaped bubbles.

We have treated the problem of four and eight point vortices in the current study for simplicity; however, the calculation is possible for any number of point vortices. As the number of point vortices increases, the more complicated interfacial motion appears. The method presented here is also applicable to the interaction between an interface and point vortices in capillary-gravity waves, if we change the initial condition for the interface and take the surface tension effect into account.[64] Those calculations, including the ones for higher Atwood numbers, will be reported elsewhere.

ACKNOWLEDGMENTS

The authors would like to thank Professor J. G. Wouchuk, Dr. F. Cobos-Campos, and Dr. T. Sano for valuable discussions. We also acknowledge Professor H. Azechi for his useful comments for experiments of RMI. This work was supported by a Grant-in-Aid for Scientific Research (C) (Grant Nos. 17K05371 and 18K03418) from the Japan Society for the Promotion of Science, the Osaka City University (OCU) Strategic Research Grant 2019 for top priority researches, and the joint research project of ILE, Osaka University.

APPENDIX: NUMERICAL SCHEMES

In this appendix, we provide the numerical schemes using the vortex method.[15,42,43,46,47,65] The discretized equation of (4), which gives the interfacial velocity, is

$$W_{s,x,j} = -\frac{h}{4\pi}\sum_{\substack{m=0\\ m\neq j}}^{N-1}\frac{\sinh(Y_j - Y_m)\gamma_m s_{e,m}}{\cosh(Y_j - Y_m) - \cos(X_j - X_m) + \delta^2},$$
$$W_{s,y,j} = \frac{h}{4\pi}\sum_{\substack{m=0\\ m\neq j}}^{N-1}\frac{\sin(X_j - X_m)\gamma_m s_{e,m}}{\cosh(Y_j - Y_m) - \cos(X_j - X_m) + \delta^2}, \tag{A1}$$

where N is the grid number in the discretization which increases as the vortex sheet grows, $h = 2\pi/N$, and δ is a regularized parameter to avoid the divergence of the integral (4),[42] When $\delta \neq 0$, the calculation of Eq. (A1) is called the vortex (blob) method.[40] Here, the variables $X_j \equiv X(e_j)$, $Y_j \equiv Y(e_j)$ and $\gamma_j \equiv \gamma(e_j)$ $(e_j = 2\pi j/N)$ are expanded into discrete Fourier series

$$X_j = e_j + \sum_{m=-N/2}^{N/2}\hat{X}_m e^{ime_j},$$
$$Y_j = \sum_{m=-N/2}^{N/2}\hat{Y}_m e^{ime_j}, \tag{A2}$$
$$\gamma_j = \sum_{m=-N/2}^{N/2}\hat{\gamma}_m e^{ime_j} \quad (j = 0, \ldots, N-1),$$

with their spectral derivatives

$$X_{e,m} = 1 + \sum_{m=-N/2}^{N/2} im\hat{X}_m e^{ime_j},$$
$$Y_{e,m} = \sum_{m=-N/2}^{N/2} im\hat{Y}_m e^{ime_j}, \tag{A3}$$
$$\gamma_{e,m} = \sum_{m=-N/2}^{N/2} im\hat{\gamma}_m e^{ime_j},$$

where $X_{e,m} = (\partial X/\partial e)_m$ and so on. Note that the derivatives (A3) do not involve errors which necessarily arise in derivative representations by usual difference approximations. The expansion (A2) is necessary to apply the Fourier filter introduced by Krasny[41,42] to eliminate the higher harmonics, where we set the filter level as 10^{-13}. The spectral derivative (A3) is introduced to solve Eq. (10) with high accuracy.

There are some methods to solve Eq. (A1) together with Eq. (10).[15,43,46,62] Here, we adopt a point insertion scheme presented by Sohn *et al.*[46] This method was first adopted for the calculation of the vortex sheet in KHI by Krasny[42] and improved by Sohn *et al.* to be able to apply to the computation of the vortex sheet with density stratification such as RMI or RTI. The same point insertion scheme is also applicable to the 3D RMI or RTI with cylindrical geometry.[65] The algorithm is as follows:[65]

1. At time t_{n+1}, we calculate $\triangle X_j^{n+1} \equiv |X_{j+1}^{n+1} - X_j^{n+1}|$ and $\triangle Y_j^{n+1} \equiv |Y_{j+1}^{n+1} - Y_j^{n+1}|$, where (X_j^n, Y_j^n) are discretized coordinates of $\boldsymbol{X} = (X, Y)$ at time t_n $(j = 1, \ldots, N;\ N$, the grid number). Then, we require that

$$d \equiv \sqrt{(\triangle X_j^{n+1})^2 + (\triangle Y_j^{n+1})^2} < d_{\lim}, \tag{A4}$$

where $d_{\lim}$ is a threshold value in the distance d on the interface. If the distance d does not satisfy the requirement (A4), we insert a point $\boldsymbol{X}_p^n = (X_p^n, Y_p^n)$ in the middle of $\boldsymbol{X}_j^n$ and $\boldsymbol{X}_{j+1}^n$ by placing it using the cubic spline (refer to Fig. 15). Note that although the requirement is calculated at time t_{n+1}, the interpolation itself is performed at time t_n.
2. We interpolate the (true) vortex sheet strength γ_p^n (this is not the strength $\gamma_{p,j}$ of point vortex j used in the body) at the new point $\boldsymbol{X}_p^n$.
3. We compute $d\gamma_p^n/dt$ and the velocity $\boldsymbol{X}_{t,p}^n$ by using Eqs. (10) and (A1).
4. We advance all marker points $\boldsymbol{X}_j^n \rightarrow \boldsymbol{X}_j^{n+1}$.

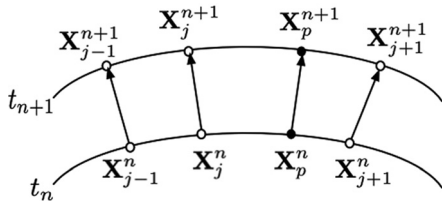

FIG. 15. Schematic figure of the point insertion scheme.

We perform from the above 1 to 4 at each time step. This is a kind of (time) corrective scheme associated with a point insertion.

Denoting the integrands in Eq. (A1) as f, the integrals (A1) are calculated by the trapezoidal rule

$$\text{P.V.}\int_{e-\pi}^{e+\pi} f(e, e')de' \rightarrow h\sum_{\substack{k=-N/2+1\\ k\neq 0}}^{N/2} f(kh),$$

when the grid number N is even, and

$$\text{P.V.}\int_{e-\pi}^{e+\pi} f(e, e')de' \rightarrow h\sum_{\substack{k=-(N+1)/2+1\\ k\neq 0}}^{(N+1)/2} f(kh),$$

for odd N (this situation can occur during the interpolation). The summation is taken symmetrically from the nearest point to the farthest point with respect to the singular point $e = 0$ to avoid the round-off error. This requirement comes from the fact that we adopt the cubic spline in the interpolation. If we use the Lagrange interpolation, we can compute the singular integral with the conventional trapezoidal rule without considering the order of the summation.

The integral equation (10) is solved iteratively under some tolerance level (10^{-11} here). Temporal integration is calculated by the fourth-order Runge–Kutta method. Since the grid number N increases as the vortex sheet evolves, we need to vary the time step in accordance with that. In the calculation, we set the time step $\triangle t$ so that $\triangle t = \triangle t_0/2^{m-1}$ for $N \geq 2^{(m-1)}N_0$ $(m = 1, 2, 3\cdots)$, where N_0 and $\triangle t_0$ are the grid number and time step at $t = 0$, respectively. We select $N_0 = 256$ and $\triangle t_0 = 0.001$ throughout the present paper.

DATA AVAILABLITY

The data that support the findings of this study are available from the corresponding author upon reasonable request.

REFERENCES

[1]W. W. Willmarth, G. Tryggvason, A. Hirsa, and D. Yu, "Vortex pair generation and interaction with a free surface," Phys. Fluids A **1**, 170–172 (1989).
[2]S. Fish, "Vortex dynamics in the presence of free surface waves," Phys. Fluids A **3**, 504–506 (1991).
[3]J. G. Telste, "Potential flow about two counter-rotating vortices approaching a free surface," J. Fluid Mech. **201**, 259–278 (1989).
[4]P. A. Tyvand, "On the interaction between a strong vortex pair and a free surface," Phys. Fluids A **2**, 1624–1634 (1990).
[5]P. A. Tyvand, "Motion of a vortex near a free surface," J. Fluid Mech. **225**, 673–686 (1991).
[6]P. D. Cummings, "The growth of wind waves estimated using a new irrotational finite amplitude water wave model," J. Coastal Res. **14**, 1354–1362 (1998).
[7]J. W. Miles, "On the generation of surface waves by shear flows," J. Fluid Mech. **3**, 185–204 (1957).
[8]V. E. Zakharov, S. I. Badulin, V. V. Geogjaev, and A. N. Pushkarev, "Weak-turbulent theory of wind-driven sea," Earth Space Sci. **6**, 540–556 (2019).
[9]E. Tochimoto, S. Yokota, H. Niino, and W. Yanase, "Mesoscale convective vortex that causes tornado-like vortices over the sea: A potential risk to maritime traffic," Mon. Weather Rev. **147**, 1989–2007 (2019).
[10]R. D. Richtmyer, "Taylor instability in shock acceleration of compressible fluids," Commun. Pure Appl. Math. **13**, 297–319 (1960).
[11]E. E. Meshkov, "Instability of the interface of two gases accelerated by a shock wave," Sov. Fluid Dyn. **4**, 101–108 (1972).
[12]R. Y. T. Inoue and S. Inutsuka, "Turbulence and magnetic field amplification in supernova remnants: Interactions between a strong shock wave and multiphase interstellar medium," Astrophys. J. **695**, 825 (2009).
[13]T. Sano, K. Nishihara, C. Matsuoka, and T. Inoue, "Magnetic field amplification associated with the Richtmyer–Meshkov instability," Astrophys. J. **758**, 126 (2012).
[14]T. Sano, T. Inoue, and K. Nishihara, "Critical magnetic field strength for suppression of the Richtmyer–Meshkov instability in plasmas," Phys. Rev. Lett. **111**, 205001 (2013).
[15]C. Matsuoka, K. Nishihara, and T. Sano, "Nonlinear dynamics of non-uniform current-vortex sheets in magnetohydrodynamic flows," J. Nonlinear Sci. **27**, 531–572 (2017).
[16]S. I. Abarzhi, A. K. Bhowmick, A. Naveh, A. Pandian, N. C. Swisher, R. F. Stellingwerf, and W. D. Arnett, "Supernova, nuclear synthesis, fluid instabilities, and interfacial mixing," Proc. Natl. Acad. Sci. U. S. A. **116**, 18184–18192 (2019).
[17]G. Dimonte, C. E. Frerking, M. Schneider, and B. Remington, "Richtmyer–Meshkov instability with strong radiatively driven shocks," Phys. Plasmas **3**, 614–630 (1996).
[18]R. L. Holmes, G. Dimonte, B. Fryxell, M. L. Gittings, J. W. W. Grove, H. Schneider, D. Sharp, A. L. Velikovich, R. Weaver, and Q. Zang, "Richtmyer–Meshkov instability growth: Experiment, simulation and theory," J. Fluid Mech. **389**, 55–79 (1999).
[19]L. H. G. Jourdan and M. Billiotte, "Density evolution within a shock accelerated gaseous interface," Phys. Rev. Lett. **78**, 452–455 (1997).
[20]M. T. F. Poggi and G. Rodriguez, "Velocity measurements in turbulent gaseous mixtures induced by Richtmyer–Meshkov instability," Phys. Fluids **10**, 2698–2700 (1998).
[21]Y. Zhou, "Rayleigh-Taylor and Richtmyer–Meshkov instability induced flow, turbulence, and mixing. I," Phys. Rep. **720-722**, 1–136 (2017).
[22]A. L. Velikovich, J. G. Wouchuk, C. H. R. de Lira, N. Melzler, S. Zalesak, and A. J. Schmitt, "Shock front distortion and Richtmyer–Meshkov-type growth caused by a small preshock nonuniformity," Phys. Plasmas **14**, 072706 (2007).
[23]J. G. Wouchuk and K. Nishihara, "Asymptotic growth in the linear Richtmyer–Meshkov instability," Phys. Plasmas **4**, 1028–1038 (1997).
[24]C. Matsuoka, K. Nishihara, and Y. Fukuda, "Nonlinear evolution of an interface in the Richtmyer–Meshkov instability," Phys. Rev. E **67**, 036301 (2003).
[25]J. G. Wouchuk, C. H. R. de Lira, and A. L. Velikovich, "Analytical linear theory for the interaction of a planar shock wave with an isotropic turbulent vorticity field," Phys. Rev. E **79**, 066315 (2009).
[26]K. Nishihara, J. G. Wouchuk, C. Matsuoka, R. Ishizaki, and V. V. Zhakhovskii, "Richtmyer–Meshkov instability: Theory of linear and nonlinear evolution," Philos. Trans. R. Soc. A **368**, 1769–1807 (2010).
[27]F. Cobos-Campos and J. G. Wouchuk, "Analytic solution for the zero-order postshock profiles when an incident planar shock hits a planar contact surface," Phys. Rev. E **100**, 033107 (2019).
[28]J. G. Wouchuk, "Growth rate of the linear Richtmyer–Meshkov instability when a shock is reflected," Phys. Rev. E **63**, 056303 (2001).
[29]G. Fraley, "Rayleigh-Taylor stability for a normal shock wave-density discontinuity interaction," Phys. Fluids **29**, 376–386 (1986).
[30]M. Stanic, R. F. Stellingwerf, J. T. Cassibry, and S. I. Abarzhi, "Scale coupling in Richtmyer–Meshkov flows induced by strong shocks," Phys. Plasmas **19**, 082706 (2012).
[31]M. Stanic, R. F. Stellingwerf, J. T. Cassibry, and S. I. Abarzhi, "Non-uniform volumetric structures in Richtmyer–Meshkov flows," Phys. Fluids **25**, 106107 (2013).
[32]M. Vandenboomgaerde, D. Souffland, C. Mariani, L. Biamino, G. Jourdan, and L. Houas, "An experimental and numerical investigation of the dependency on the initial conditions of the Richtmyer–Meshkov instability," Phys. Fluids **26**, 024109 (2014).
[33]Z. Dell, R. F. Stellingwerf, and S. I. Abarzhi, "Effect of initial perturbation amplitude on Richtmyer–Meshkov flows induced by strong shocks," Phys. Plasmas **22**, 092711 (2015).
[34]F. Cobos-Campos and J. G. Wouchuk, "Analytical scalings of the linear Richtmyer–Meshkov instability when a shock is reflected," Phys. Rev. E **93**, 053111 (2016).
[35]F. Cobos-Campos and J. G. Wouchuk, "Analytical scalings of the linear Richtmyer–Meshkov instability when a rarefaction is reflected," Phys. Rev. E **96**, 013102 (2017).
[36]J. G. Wouchuk and K. Nishihara, "Linear perturbation growth at a shocked interface," Phys. Plasmas **3**, 3761–3776 (1996).
[37]J. Lindl, *Inertia Confinement Fusion: The Quest for Ignition and High Gain Using Indirect Drive* (Springer and AIP, New York, 1997).
[38]S. Atzeni and J. Meyer-ter-Vehn, *The Physics of Inertial Fusion* (Oxford Science Publications, Oxford, 2004).
[39]A. Nikroo and D. Woodhouse, "Bounce coating induced domes on glow discharge polymer coated shells," Fusion Technol. **35**, 202–205 (1999).
[40]G.-H. Cottet and P. D. Koumoutsakos, *Vortex Methods: Theory and Practice* (Cambridge University Press, Cambridge, 2000).
[41]R. Krasny, "A study of singularity formation in a vortex sheet by the point vortex approximation," J. Fluid Mech. **167**, 65–93 (1986).
[42]R. Krasny, "Computation of vortex sheet roll-up in the Trefftz plane," J. Fluid Mech. **184**, 123–155 (1987).
[43]C. Matsuoka and K. Nishihara, "Vortex core dynamics and singularity formations in incompressible Richtmyer–Meshkov instability," Phys. Rev. E **73**, 026304 (2006).
[44]C. Matsuoka and K. Nishihara, "Fully nonlinear evolution of a cylindrical vortex sheet in incompressible Richtmyer–Meshkov instability," Phys. Rev. E **73**, 055304(R) (2006).
[45]C. Matsuoka and K. Nishihara, "Analytical and numerical study on a vortex sheet in incompressible Richtmyer–Meshkov instability in cylindrical geometry," Phys. Rev. E **74**, 066303 (2006).
[46]S.-I. Sohn, D. Yoon, and W. Hwang, "Long-time simulations of the Kelvin–Helmholtz instability using an adaptive vortex method," Phys. Rev. E **82**, 046711 (2010).
[47]S.-I. Sohn, "Late-time vortex dynamics of Rayleigh–Taylor instability," J. Phys. Soc. Jpn. **80**, 084401 (2011).
[48]H. Lamb, *Hydrodynamics* (Dover, New York, 1932).
[49]P. K. Newton, *The N-Vortex Problem* (Springer, New York, 2000).
[50]M. J. Ablowitz, A. S. Fokas, and Z. H. Musslimani, "On a new non-local formulation of water waves," J. Fluid Mech. **562**, 313–343 (2006).

[51]C. W. Curtis and H. Kalisch, "Vortex dynamics in nonlinear free surface flows," Phys. Fluids **29**, 032101 (2017).
[52]N. Zabusky, "Vortex paradigm for accelerated inhomogeneous flows: Visiometrics for the Rayleigh-Taylor and Richtmyer–Meshkov environments," Annu. Rev. Fluid Mech. **31**, 495–536 (1999).
[53]Q. Zhang and S. I. Sohn, "An analytical nonlinear theory of Richtmyer–Meshkov instability," Phys. Lett. A **212**, 149–155 (1996).
[54]Q. Zhang and S. I. Sohn, "Nonlinear theory of unstable fluid mixing driven by shock wave," Phys. Fluids **9**, 1106–1124 (1997).
[55]K. Mikaelian, "Freeze-out and the effect of compressibility in the Richtmyer–Meshkov instability," Phys. Fluids **6**, 356–368 (1994).
[56]J. G. Wouchuk, "Growth rate of the Richtmyer–Meshkov instability when a rarefaction is reflected," Phys. Plasmas **8**, 2890–2907 (2001).
[57]G. Birkhoff, "Helmholtz and Taylor instability," Proc. Symp. Appl. Math. Soc. **13**, 55–76 (1962).
[58]N. Rott, "Diffraction of a weak shock with vortex generation," J. Fluid Mech. **1**, 111–128 (1956).
[59]P. G. Saffman, *Vortex Dynamics* (Cambridge University Press, Cambridge, 1992).
[60]D. I. Pullin, "Numerical studies of surface-tension effects in nonlinear Kelvin-Helmholtz and Rayleigh–Taylor instability," J. Fluid Mech. **119**, 507–532 (1982).
[61]G. Baker, D. I. Meiron, and S. A. Orszag, "Generalized vortex methods for free surface flow problems," J. Fluid Mech. **123**, 477–501 (1982).
[62]R. M. Kerr, "Simulation of Rayleigh–Taylor flows using vortex blobs," J. Comput. Phys. **76**, 48–84 (1988).
[63]J. W. Jacobs and J. M. Sheeley, "Experimental study of incompressible Richtmyer–Meshkov instability," Phys. Fluids **8**, 405–415 (1996).
[64]C. Matsuoka, "Vortex sheet motion in incompressible Richtmyer–Meshkov and Rayleigh–Taylor instabilities with surface tension," Phys. Fluids **21**, 092107 (2009).
[65]C. Matsuoka, "Three-dimensional vortex sheet motion with axial symmetry in incompressible Richtmyer–Meshkov and Rayleigh–Taylor instabilities," Phys. Scr. **T155**, 014013 (2013).